ON THE RELATIONSHIP BETWEEN A HOT-CHANNEL-LIKE SOLAR MAGNETIC FLUX ROPE AND ITS EMBEDDED PROMINENCE

X. CHENG[1,2,3], M. D. DING[1,3], J. ZHANG[1,4], A. K. SRIVASTAVA[5], Y. GUO[1,3], P. F. CHEN[1,3], AND J. Q. SUN[1,3]

[1] School of Astronomy and Space Science, Nanjing University, Nanjing 210093, China; xincheng@nju.edu.cn
[2] State Key Laboratory of Space Weather, Chinese Academy of Sciences, Beijing 100190, China
[3] Key Laboratory for Modern Astronomy and Astrophysics (Nanjing University), Ministry of Education, Nanjing 210093, China
[4] School of Physics, Astronomy and Computational Sciences, George Mason University, Fairfax, VA 22030, USA
[5] Department of Physics, Indian Institute of Technology (IIT)-BHU, Varanasi-221005, India

ABSTRACT

A magnetic flux rope (MFR) is a coherent and helical magnetic field structure that has recently been found likely to appear as an elongated hot channel prior to a solar eruption. In this Letter, we investigate the relationship between the hot channel and the associated prominence through analysis of a limb event on 2011 September 12. In the early rise phase, the hot channel was initially cospatial with the prominence. It then quickly expanded, resulting in a separation of the top of the hot channel from that of the prominence. Meanwhile, they both experienced an instantaneous morphology transformation from a Λ shape to a reversed-Y shape and the top of these two structures showed an exponential increase in height. These features are a good indication of the occurrence of kink instability. Moreover, the onset of kink instability is found to coincide in time with the impulsive enhancement of flare emission underneath the hot channel, suggesting that ideal kink instability likely also plays an important role in triggering fast flare reconnection besides initiating the impulsive acceleration of the hot channel and distorting its morphology. We conclude that the hot channel is most likely the MFR system and the prominence only corresponds to the cool materials that are collected in the bottom of the helical field lines of the MFR against gravity.

Key words: Sun: corona – Sun: coronal mass ejections (CMEs) – Sun: filaments, prominences – Sun: magnetic fields

Online-only material: animations, color figures

1. INTRODUCTION

A magnetic flux rope (MFR) is a coherent magnetic structure with magnetic field lines wrapping around its central axis. This structure has been used as a significant configuration for studying the initiation mechanisms of solar energetic phenomena, including flares, prominences (or filaments when seen on the solar disk), and coronal mass ejections (CMEs; e.g., Fan & Gibson 2004; Török & Kliem 2005; Kliem & Török 2006; Aulanier et al. 2010; Olmedo & Zhang 2010; Leake et al. 2013; Nishida et al. 2013). Current models can be largely grouped into two categories based on whether or not magnetic reconnection is involved in the destabilization process. One category is the reconnection type, including inner tether-cutting (Moore et al. 2001) and top/lateral breakout reconnections (Antiochos et al. 1999; Chen & Shibata 2000). The other type is ideal magneto-hydrodynamic instabilities of the MFR, including torus instability (Kliem & Török 2006) and/or kink instability (Hood & Priest 1981). Torus instability occurs if the restoring force of the MFR caused by the background field decreases faster than the outward-directed Lorenz self-force as the MFR expands (Kliem & Török 2006; Olmedo & Zhang 2010). Kink instability refers to the helical instability of the MFR which takes place if the average twist number of the MFR exceeds a threshold (Török et al. 2004; Srivastava et al. 2010).

Due to the theoretical importance of the MFR, researchers are concerned with the question of whether the MFR exists prior to eruption. Indirect evidence supporting the pre-existence of the MFR has previously been uncovered, for example, forward or reverse S-shaped sigmoids (Rust & Kumar 1996; Canfield et al. 1999; Tripathi et al. 2009) and dark cavities (Low & Hundhausen 1995; Gibson et al. 2004; Dove et al. 2011; Bak-Stȩślicka et al. 2013). Filaments are also thought to be evidence of the pre-existence of MFR because they often correspond well to the dips of the helical lines in extrapolated nonlinear force-free field configurations (e.g., Mackay et al. 2010; Guo et al. 2010; Su et al. 2011). Recently, utilizing the Atmospheric Imaging Assembly (AIA; Lemen et al. 2012) telescope on board the *Solar Dynamics Observatory* (*SDO*), Zhang et al. (2012) and Cheng et al. (2013a) discovered another important structure: a coherently elongated and S-shaped hot channel. The channel appears above the neutral line of the active region tens of minutes before the eruption and is only visible in the AIA 131 Å and 94 Å passbands, showing high temperatures of ⩾8 MK. As the hot channel ascends, its morphology quickly transforms into a loop-like shape. However, during the transformation process, the two footpoints remain fixed in the photosphere. With the channel expanding and rising, a CME quickly builds up in the very low corona (also see; Liu et al. 2010; Cheng et al. 2013b; Patsourakos et al. 2013; Li & Zhang 2013a). These results strongly suggest that the hot channel is most likely to be the MFR. In this Letter, we further investigate the relationship between the hot channel and the associated prominence through a detailed analysis of a limb event on 2011 September 12. In Section 2, we show data reduction and results, followed by the summary and discussions in Section 3.

2. OBSERVATIONS AND RESULTS

2.1. Heating and Eruption of the Prominence

On 2011 September 12, a prominence erupted above the east limb of the Sun. Its early evolution was well captured by the
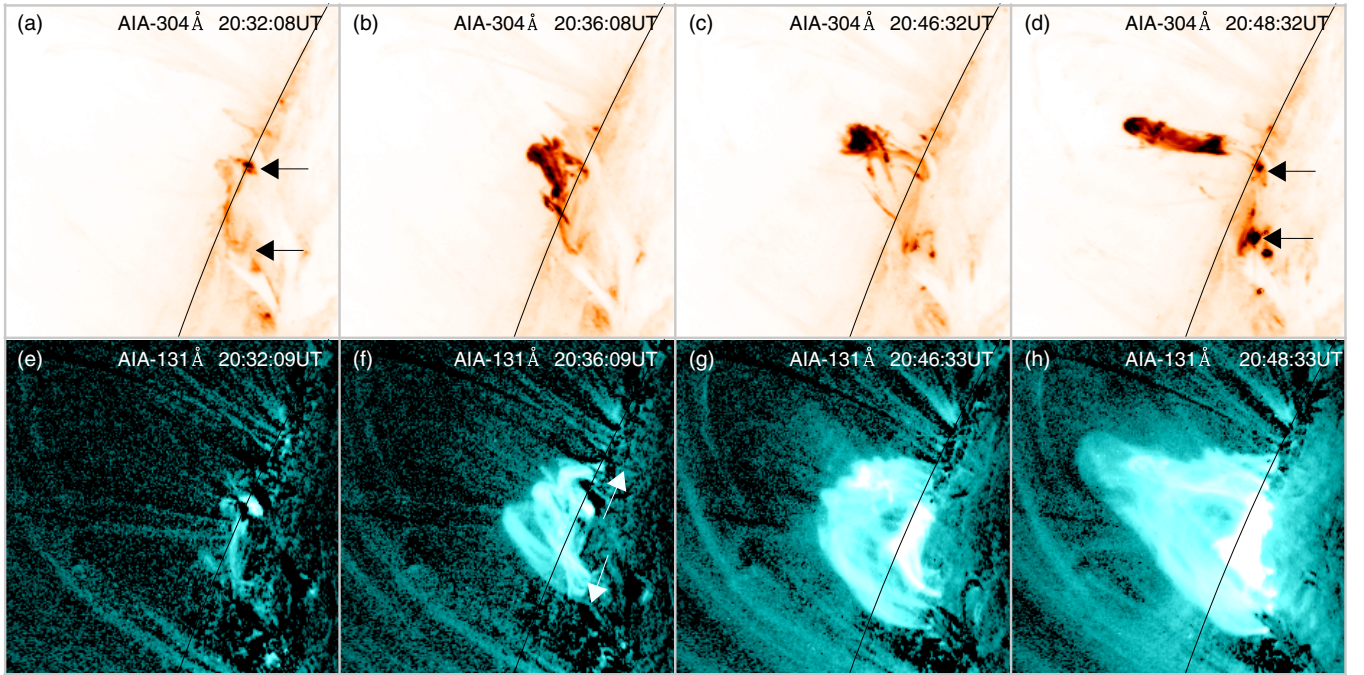
Figure 1. (a)–(d) *SDO*/AIA 304 Å (∼0.05 MK) (negative intensity) images displaying the heating and eruption of the prominence on 2011 September 12. Two black arrows in panel (a) and (e) indicate the two footpoints of the prominence. (e)–(h) *SDO*/AIA 131 Å (∼0.4 MK and 11.0 MK) base-difference images, with the base image at 20:20 UT showing the heating and eruption of the hot channel. Two white arrows in panel (f) point out the extension of the hot-channel footpoints in the early phase. The black line in each panel corresponds to the solar limb.

(Animations and a color version of this figure are available in the online journal.)

SDO/AIA due to its high spatial resolution (1″2), high temporal cadence (12 s), and multi-temperature (0.06–20 MK; O'Dwyer et al. 2010) ability. Tripathi et al. (2013) studied this prominence but concentrated on its partial eruption. Here, we focus on the relationship between the prominence and the associated hot-channel-like MFR. The early activation can clearly be seen from the AIA 304 Å images (Figures 1(a) and (b)). Initially, the prominence lay low above the solar surface with the two footpoints anchored in the chromosphere (Figure 1(a)). Probably due to reconnection, indicated by EUV brightenings along the prominence and the slight enhancement of the *GOES* soft X-ray (SXR) 1–8 Å flux (also see Tripathi et al. 2013), the prominence started to rise slowly after ∼20:30 UT (Figure 1(b)). At ∼20:46 UT, the prominence suddenly exhibited an impulsive acceleration. The morphology evolved instantaneously from a Λ shape to a reverse-Y shape (Figures 1(c) and (d)), from which we infer the occurrence of kink instability (e.g., Török & Kliem 2005). However, probably due to the fact that some materials drained down to the chromosphere, the left part of the reversed-Y shape became invisible after ∼20:48 UT. Moreover, at ∼20:46 UT, the brightness at the projected crossing point of the two legs of the prominence increased to maximum in all AIA EUV passbands (Figure 1(c)). This implies that magnetic reconnection took place there. Subsequently, the EUV brightenings were also enhanced at the two footpoints of the prominence (Figure 1(d)), indicating that reconnection also heats the chromosphere.

2.2. Heating and Eruption of the Hot-channel-like MFR

We find that the erupted prominence was closely associated with an elongated hot-channel-like structure. In the first several minutes, some diffuse threads, similar to the prominence,

were visible in the AIA 131 Å passbands (Figure 1(e)). As time elapsed, probably due to reconnection heating, more and more threads revealed themselves. At 20:36 UT (Figure 1(f)), all of the threads seemed to converge. At 20:46 UT, the whole system formed a well-shaped and coherent channel-like structure (Figure 1(g)). As has been revealed in previous studies (Zhang et al. 2012; Cheng et al. 2013a; Patsourakos et al. 2013), the structure can only be seen in the AIA high temperature passbands, i.e., 131 Å and 94 Å, but not in the other cooler wavelengths. This shows that the channel must have a temperature of ⩾8 MK.

An interesting discovery is that the hot channel was initially almost co-aligned with the prominence in space, but later on the top of the hot channel separated from that of the prominence (Figures 2(a)–(c)). In particular, at ∼20:48 UT, the prominence was only cospatial with the bottom of the right part of the hot channel (Figure 2(d)). The results can be interpreted as a general scenario wherein the hot channel is likely the MFR and the prominence is only the collection of cool materials at the bottom of the MFR; the eruption of the prominence was essentially followed by that of the MFR. Moreover, the hot channel also displayed a morphology transformation similar to the prominence. From ∼20:46 UT, the top of the hot channel started to arch upward. In the period of 20:46–20:48 UT, the arching first made the hot channel take on a Λ shape (Figure 2(c)), which then quickly evolved into a reverse-Y shape (Figures 1(h) and 2(d)).

As the morphology of the hot channel transitioned from Λ to reverse-Y shape, flare-related reconnection began to dominate the whole heating process. We calculate the differential emission measure (DEM) of the erupted structure using the SolarSoft routine "xrt_dem_iterative2.pro" (Cheng et al. 2012). With the DEM results, we then construct
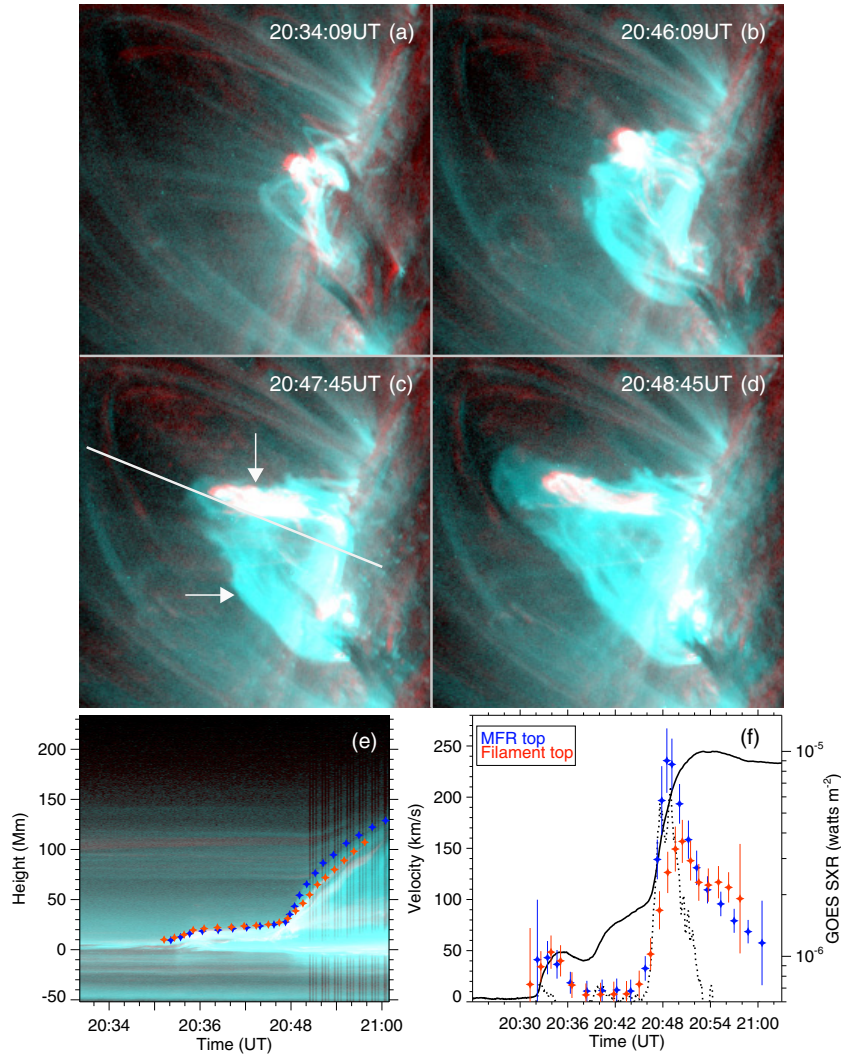
Figure 2. (a)–(d) Composite AIA 131 Å (∼0.4 MK and 11.0 MK) and 304 Å (∼0.05 MK) images showing the spatial relationship between the hot channel (blue) and the associated prominence (light red) before and during eruption. (e) Stack plot of the AIA 131 Å and 304 Å composite intensity along the slice as shown by the white oblique line in panel (c). Blue and red stars indicate the height measurements of the hot channel and prominence above the solar surface, respectively. (f) Velocity evolution of the hot channel (blue) and prominence (red). The solid and dotted curves denote the *GOES* 1–8 Å SXR flux of the associated flare and its time derivative, respectively.

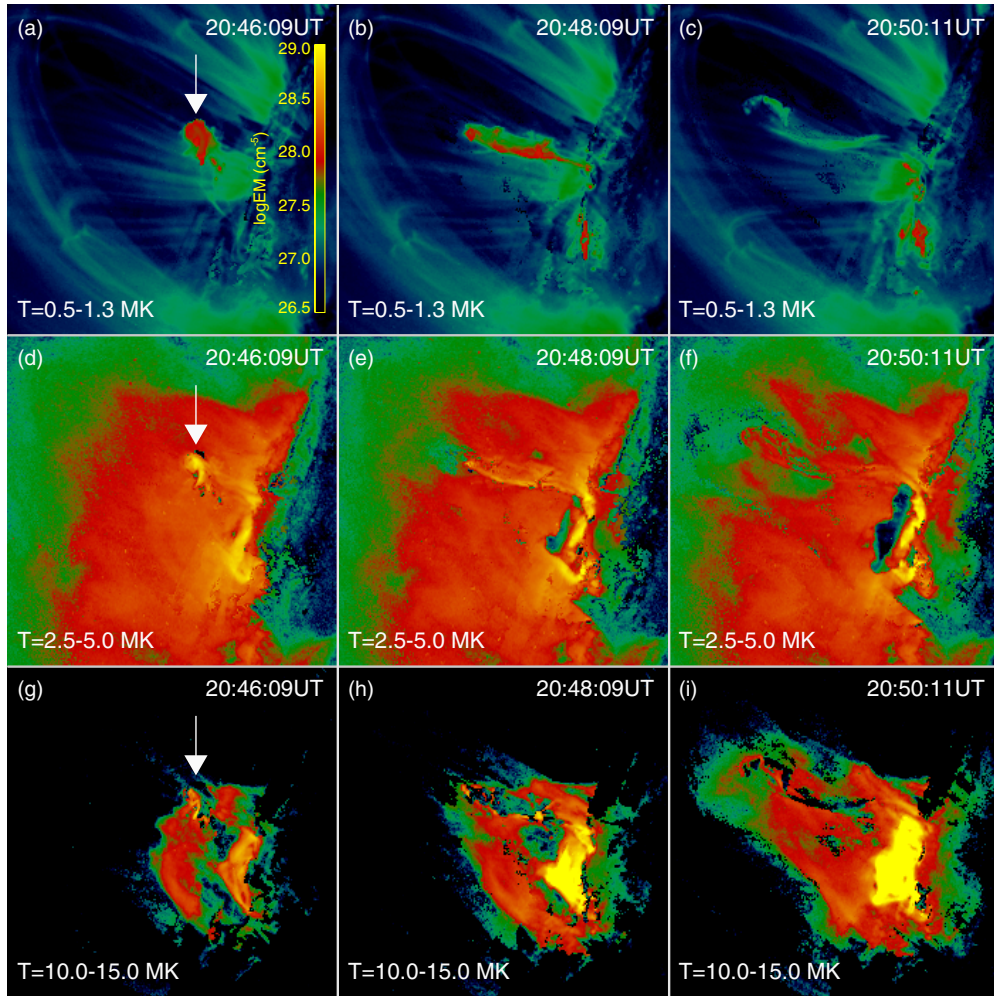(An animation and a color version of this figure are available in the online journal.)

two-dimensional maps of the emission measure (EM) of the plasma in different temperature intervals (ΔT) through the formula $\mathrm{EM}(T) = \int_{T-\Delta T}^{T} \mathrm{DEM}(T')\mathrm{d}T'$.

Figure 3 shows the EM structures of the eruption in three temperature intervals. It can be seen that at ∼20:46 UT, the plasma in the space occupied by the prominence showed emission in all temperatures (0.5–5 MK) while the surrounding hot channel only exhibited emission from the hot plasma (10–15 MK). This reveals that the hot channel was heated to high temperatures at that time. We suggest that slow magnetic reconnection probably occurs inside or around the hot channel to heat and build up the channel before ∼20:46 UT; however, this reconnection is too weak to generate nonthermal particles, and thus is different from the fast flare reconnection in the later phase (also see Aulanier et al. 2010; Cheng et al. 2013b; Guo et al. 2013). After 20:46 UT, the hot channel still had a temperature of >8 MK and the prominence had a temperature of <5 MK; however, the EM of both the hot channel and the prominence tended to decrease, mainly due to expansion. On the other hand, the EM of the flare region underneath the hot

channel was quickly enhanced. In particular, for the hot plasma, the EM increased from ∼10^{28} cm^{-5} at 20:47 UT to ∼10^{29} cm^{-5} at 20:50 UT in the low-lying flare region. This indicates that the morphology transformation of the hot channel is also associated with the triggering of the fast flare reconnection that may further help to heat and build up the hot channel.

2.3. Kinematical Relationship between the Hot-channel-like MFR and Prominence

In this section, we study the kinematics of the hot-channel-like MFR and the prominence in detail. We take a slice along the direction of the eruption (Figure 2(c)). The time sequence of the slice makes a stack plot. Using the stack plot, we measure the heights of the hot channel and the associated prominence. Applying a first-order piecewise numerical derivative to the height–time data, we derive the velocities of the hot channel and prominence. The uncertainties in the velocities arise from the uncertainties in the height measurements, which are estimated to be 4 pixel sizes (∼1.7 Mm).

Figure 3. Two-dimensional EM maps of the hot channel and associated prominence in different temperature intervals. The white arrows denote that the cross part of the prominence has the biggest EM value.

(An animation and a color version of this figure are available in the online journal.)

Figures 2(e) and (f) display the height and velocity profiles of the hot channel and prominence. One can observe that the hot channel experienced two distinct phases: a slow rise phase of 20 minutes and an impulsive acceleration phase of only ~5 minutes. During the first several minutes, the height of the hot channel increased from ~10 Mm at 20:30 UT to ~20 Mm at 20:36 UT, resulting in an average velocity of ~30 km s^{-1}. The early rise process corresponds well to the brightening along the hot channel and prominence, confirming that their activation was most likely the result of slow reconnection. In the period ~10 minutes after 20:36 UT, the rise of the hot channel tended to slow down; the height only increased to 25 Mm at ~20:46 UT, corresponding to an average velocity of ~10 km s^{-1} (Figure 2(f)).

An important result is that the height evolution of the hot channel had an apparent jump (Figure 2(e)). Correspondingly, the velocity impulsively increased around the jump, e.g., from ~10 km s^{-1} at ~20:46 UT to ~250 km s^{-1} 3 minutes later at ~20:49 UT (Figure 4(b)). The average acceleration in this period is estimated to be ~1300 m s^{-2}, which is much larger than the average acceleration (330 m s^{-2}) of the impulsive CMEs (e.g., Zhang & Dere 2006). After ~20:49 UT, the velocity started to decrease gradually and became to be ~50 km s^{-1} at ~21:00 UT with an average deceleration of ~300 m s^{-2}. This deceleration

led to a failed eruption, as is evident from the lack of propagating CME in the white-light coronagraph images. In order to exactly estimate the onset time of the impulsive acceleration, we use a function consisting of both a linear and an exponential component to fit the height–time measurements of the hot channel from 20:36 UT to 20:48 UT. The details of the technique can be found in Cheng et al. (2013b). From Figures 4(a) and (b), one can see that the height of the hot channel is well described by a combination of the linear and exponential functions. The exponential component is believed to be a fundamental feature of the MFR eruption trajectory driven by kink instability (e.g., Török & Kliem 2005; Schrijver et al. 2008). Assuming that the hot channel is impulsively accelerated at the time when the velocity of the exponential component is equal to that of the linear component, the impulsive acceleration onset is found to be at 20:45:40 UT with an uncertainty of 1.7 minutes, almost perfectly coincident with the sudden transformation of the hot-channel morphology from the Λ shape to reverse-Y shape. These results indicate that the hot channel most likely underwent kink instability, thus triggering and driving impulsive acceleration in a very short period, simultaneously distorting the axis of the hot channel, revealing a transformation of the morphology.

As for the prominence, the evolution of the height and velocity had exactly the same trends as the hot channel, however,
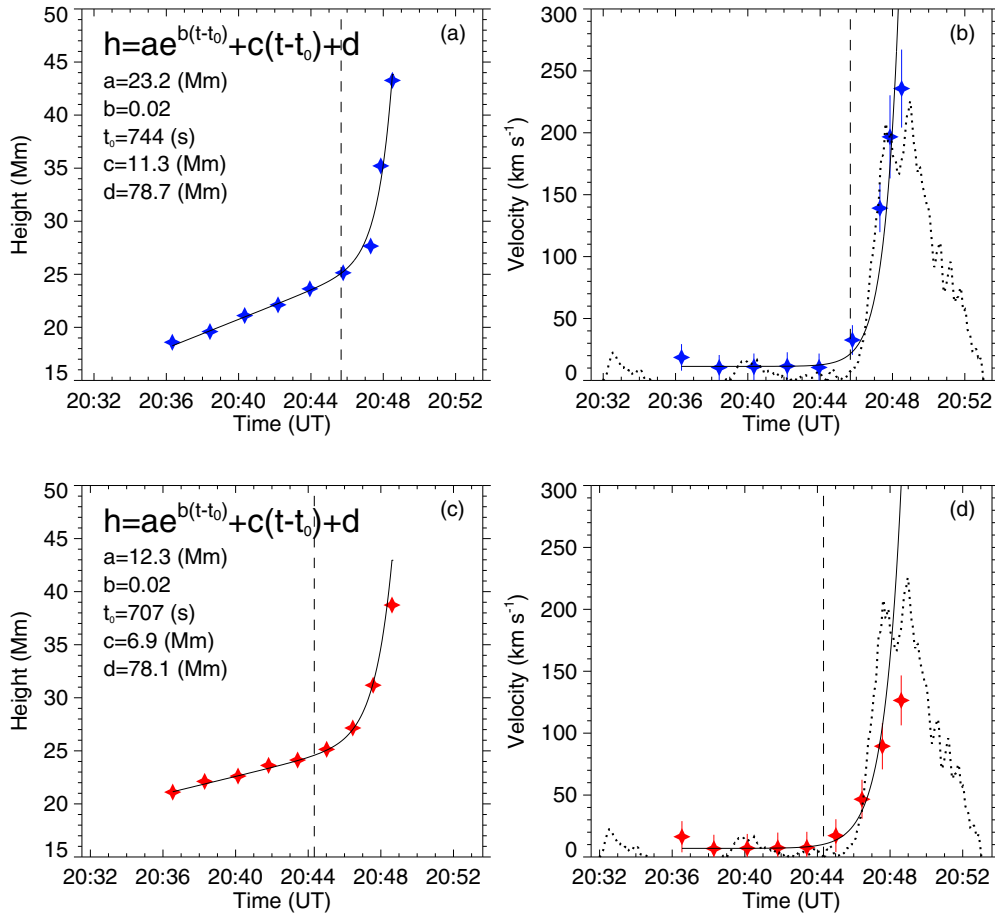
Figure 4. (a) and (b) Best fit of the height and velocity of the hot channel, as shown by the solid lines. The fitting function and resulting parameters are displayed in the top left corner. (c) and (d) Same as (a) and (b), but for the prominence. The dotted line shows the *GOES* derivative and the two vertical dashed lines show the onset time of the impulsive acceleration.

(A color version of this figure is available in the online journal.)

with some difference in magnitude. In the slow rise phase, the prominence retained the same height and linear velocity as the hot channel. With impulsive acceleration commencing, the height of the prominence also exponentially increased (Figure 4(c)). Using the same technique, we are able to fit the height variation of the prominence very well with a combination of the linear and exponential functions. The onset of the prominence impulsive acceleration is determined to occur at 20:44:20 UT with an uncertainty of 5.0 minutes (Figure 4(d)), nearly coinciding with that of the hot channel. On the other hand, we find that the height and velocity of the prominence increased more slowly than those of the hot channel shortly after the beginning of the impulsive acceleration. These results suggest that the prominence and hot channel share the same MFR system throughout the course of the eruption. Most likely, the hot channel is the MFR and the prominence corresponds to the dips of the helical field lines of the MFR. Prior to and during the slow rise phase, the MFR remains small and compact, and thus almost cospatial with the prominence (Figure 2(a)); the distance between the MFR top and prominence is too small to be recognizable. In the acceleration phase, as a result of fast reconnection, represented by the peak of the time derivative of the *GOES* SXR flux (Figure 2(f)), the newly formed high temperature poloidal flux quickly envelops the MFR, resulting in heating of the MFR and a separation between the tops of the MFR and the prominence; thus, the upper part of the MFR is only visible in the AIA high-temperature passbands (131 Å and

94 Å), while the lower part is seen in all AIA passbands because this part consists of both the cool core and the hot shell of the MFR (Figures 2(c) and (d)).

Moreover, the onset of hot channel and prominence impulsive acceleration was almost coincident with the rapid enhancement of flare emission (Figures 4(b) and (d)). Through inspection of the AIA images, we find that the strongest brightening appeared at the crossing point of the two legs of the hot channel and prominence at the onset time (∼20:46 UT; Figure 1(c) and the left column of Figure 3). With the hot channel and prominence ascending, the brightening underneath them was also rapidly increased, showing that fast reconnection started which rapidly increased the flare emission and formed the flare loops (Figures 1(g) and (h), and 3(h) and (i)). The transition of brightening from the crossing part to underneath the hot channel and prominence implies that kink instability may also have a role in causing fast flare reconnection.

3. SUMMARY AND DISCUSSION

In this Letter, we investigate the relationship between the hot channel and the associated prominence. The cospatiality of the prominence with the hot channel in the early phase (Figure 5(a)) and the following separation of the top of the hot channel from that of the prominence in the later phase (Figure 5(b)) strongly support our previous conjecture that the hot channel is likely an MFR whose lower part, i.e., the dipped part of the
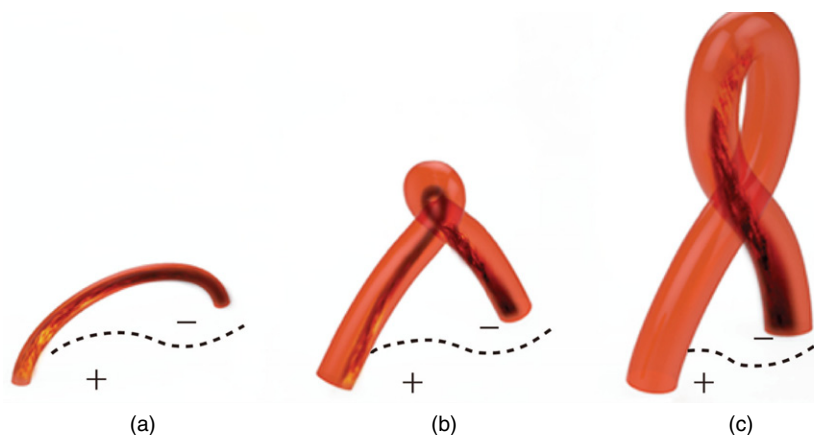
Figure 5. Schematic drawing of the relationship between the hot-channel-like MFR (red tubes) and the embedded prominence (dark materials) during early evolution. (a) Pre-eruption structure displaying the cospatiality of the MFR and prominence. (b) Separation of the MFR top from the prominence. (c) Morphology transformation of the MFR from a Λ shape to a reverse-Y shape as a result of kink instability. The dashed curve in each panel shows the polarity inverse line.

(A color version of this figure is available in the online journal.)

helical magnetic lines, corresponds to the prominence. Using the high cadence AIA data, we find that both of their evolutions experienced two phases: a slow rise phase and an impulsive acceleration phase. The evolution near the transition from the slow rise phase to the impulsive acceleration phase can be well described by a combination of linear and exponential functions. Moreover, the kinematic transition in time coincided with the quick morphological transformation from Λ shape to reverse-Y shape (Figure 5(c)). These results indicate that the hot channel most likely underwent kink instability, thus triggering the impulsive acceleration of the MFR and the fast reconnection producing the flare.

It has been recognized that the impulsive acceleration of the MFR might be triggered by torus instability (Kliem & Török 2006; Fan & Gibson 2007; Aulanier et al. 2010; Olmedo & Zhang 2010; Savcheva et al. 2012; Cheng et al. 2013b, 2014; Zuccarello et al. 2014). To tentatively study this possibility, we calculate the three-dimensional magnetic field structure using the magnetic data on 2011 September 17 provided by the Helioseismic and Magnetic Imager (Schou et al. 2012). We find that the decay index of the background field at the onset heights of the hot channel and prominence impulsive acceleration ($\sim 25.2 \pm 4.3$ Mm and $\sim 25.2 \pm 6.3$ Mm) is only ~ 1.1, which is smaller than the threshold of the torus instability (1.5; Kliem & Török 2006); thus, the torus instability is unlikely the cause of eruption in this event.

The kink instability of the hot channel requires a strong twist, thus reinforcing its physical nature as an MFR. Theoretically, the kink instability occurs when the twist number of the MFR is larger than the critical value of 1.5 (3.0π in twist angle) for an arched MFR (Fan & Gibson 2003; Török et al. 2004), or at least the threshold of 1.25 for a line-tied cylindrical MFR (Hood & Priest 1979, 1981). This can be considered as additional evidence for the existence of the MFR as the hot channel as well as being visually identified as a bundle of helical threads (e.g., Cheng et al. 2014; Li & Zhang 2013b). Finally, it is worth mentioning that although Tripathi et al. (2013) studied the same event, they concentrated on the partial eruption of the prominence. Here, we pay more attention to the relationship between the hot channel and the prominence, and conclude that the hot channel and prominence are two components of the same MFR system that simultaneously rise, accelerate, and deform, subject to kink instability.

REFERENCES

Antiochos, S. K., DeVore, C. R., & Klimchuk, J. A. 1999, ApJ, 510, 485
Aulanier, G., Török, T., Démoulin, P., & DeLuca, E. E. 2010, ApJ, 708, 314
Bak-Stęślicka, U., Gibson, S. E., Fan, Y., et al. 2013, ApJL, 770, L28
Canfield, R. C., Hudson, H. S., & McKenzie, D. E. 1999, GeoRL, 26, 627
Chen, P. F., & Shibata, K. 2000, ApJ, 545, 524
Cheng, X., Ding, M. D., Guo, Y., et al. 2014, ApJ, 780, 28
Cheng, X., Zhang, J., Ding, M. D., Liu, Y., & Poomvises, W. 2013a, ApJ, 763, 43
Cheng, X., Zhang, J., Ding, M. D., et al. 2013b, ApJL, 769, L25
Cheng, X., Zhang, J., Saar, S. H., & Ding, M. D. 2012, ApJ, 761, 62
Dove, J. B., Gibson, S. E., Rachmeler, L. A., Tomczyk, S., & Judge, P. 2011, ApJL, 731, L1
Fan, Y., & Gibson, S. E. 2003, ApJL, 589, L105
Fan, Y., & Gibson, S. E. 2004, ApJ, 609, 1123
Fan, Y., & Gibson, S. E. 2007, ApJ, 668, 1232
Gibson, S. E., Fan, Y., Mandrini, C., Fisher, G., & Demoulin, P. 2004, ApJ, 617, 600
Guo, Y., Ding, M. D., Cheng, X., Zhao, J., & Pariat, E. 2013, ApJ, 779, 157
Guo, Y., Schmieder, B., Démoulin, P., et al. 2010, ApJ, 714, 343
Hood, A. W., & Priest, E. R. 1979, SoPh, 64, 303
Hood, A. W., & Priest, E. R. 1981, GApFD, 17, 297
Kliem, B., & Török, T. 2006, PhRvL, 96, 255002
Leake, J. E., Linton, M. G., & Török, T. 2013, ApJ, 778, 99
Lemen, J. R., Title, A. M., Akin, D. J., et al. 2012, SoPh, 275, 17
Li, L. P., & Zhang, J. 2013a, A&A, 552, L11
Li, T., & Zhang, J. 2013b, ApJL, 778, L29
Liu, R., Liu, C., Wang, S., Deng, N., & Wang, H. 2010, ApJL, 725, L84
Low, B. C., & Hundhausen, J. R. 1995, ApJ, 443, 818
Mackay, D. H., Karpen, J. T., Ballester, J. L., Schmieder, B., & Aulanier, G. 2010, SSRv, 151, 333
Moore, R. L., Sterling, A. C., Hudson, H. S., & Lemen, J. R. 2001, ApJ, 552, 833
Nishida, K., Nishizuka, N., & Shibata, K. 2013, ApJL, 775, L39
O'Dwyer, B., Del Zanna, G., Mason, H. E., Weber, M. A., & Tripathi, D. 2010, A&A, 521, A21
Olmedo, O., & Zhang, J. 2010, ApJ, 718, 433
Patsourakos, S., Vourlidas, A., & Stenborg, G. 2013, ApJ, 764, 125
Rust, D. M., & Kumar, A. 1996, ApJL, 464, L199

Savcheva, A., Pariat, E., van Ballegooijen, A., Aulanier, G., & DeLuca, E. 2012, ApJ, 750, 15

Schou, J., Scherrer, P. H., Bush, R. I., et al. 2012, SoPh, 275, 229

Schrijver, C. J., Elmore, C., Kliem, B., Török, T., & Title, A. M. 2008, ApJ, 674, 586

Srivastava, A. K., Zaqarashvili, T. V., Kumar, P., & Khodachenko, M. L. 2010, ApJ, 715, 292

Su, Y., Surges, V., van Ballegooijen, A., DeLuca, E., & Golub, L. 2011, ApJ, 734, 53

Török, T., & Kliem, B. 2005, ApJL, 630, L97

Török, T., Kliem, B., & Titov, V. S. 2004, A&A, 413, L27

Tripathi, D., Kliem, B., Mason, H. E., Young, P. R., & Green, L. M. 2009, ApJL, 698, L27

Tripathi, D., Reeves, K. K., Gibson, S. E., Srivastava, A., & Joshi, N. C. 2013, ApJ, 778, 142

Zhang, J., Cheng, X., & Ding, M.-D. 2012, NatCo, 3, 747

Zhang, J., & Dere, K. P. 2006, ApJ, 649, 1100

Zuccarello, F. P., Seaton, D. B., Mierla, M., et al. 2014, ApJ, 785, 88